

Electronic excitations in γ -Li₂IrO₃

Ying Li, Stephen M. Winter, Harald O. Jeschke, and Roser Valentí
*Institut für Theoretische Physik, Goethe-Universität Frankfurt,
 Max-von-Laue-Strasse 1, 60438 Frankfurt am Main, Germany*
 (Dated: November 21, 2016)

We investigate the electronic properties of the three-dimensional stripy honeycomb γ -Li₂IrO₃ via relativistic density functional theory calculations as well as exact diagonalization of finite clusters and explore the details of the optical conductivity. Our analysis of this quantity reveals the microscopic origin of the experimentally observed (i) optical transitions and (ii) anisotropic behavior along the various polarization directions. In particular we find that the optical excitations are overall dominated by transitions between $j_{\text{eff}} = 1/2$ and $3/2$ states and the weight of transitions between $j_{\text{eff}} = 1/2$ states at low frequencies can be correlated to deviations from a pure Kitaev description. We furthermore reanalyze within this approach the electronic excitations in the known two-dimensional honeycomb systems α -Li₂IrO₃ and Na₂IrO₃ and discuss the results in comparison to γ -Li₂IrO₃.

I. INTRODUCTION

The two-dimensional honeycomb iridates Na₂IrO₃ and α -Li₂IrO₃ have been suggested as candidate materials for the realization of bond-dependent anisotropic interactions as described by the Kitaev model¹. The appropriate description of the electronic structure of these materials is currently being discussed. In the limit of strong spin-orbit coupling (SOC) and electron-electron interactions, the low-energy degrees of freedom are predicted to be localized spin-orbital doublet $j_{\text{eff}} = 1/2$ states^{2–7}. These localized moments are thought to persist despite relatively weak correlations in the $5d$ Ir orbitals due to an effective bandwidth reduction via SOC. That is, once SOC is included, the highest occupied $j_{\text{eff}} = 1/2$ bands become very narrow, enhancing the role of correlations. A complementary perspective was also given from the limit of weak correlations. In this case, the electronic properties of these systems can be described in terms of a recently proposed quasimolecular orbital (QMO) basis^{8–10}. When SOC is included in this picture, a (pseudo)gap was found at the Fermi energy for Na₂IrO₃, suggesting the material is relatively close to a band insulating state in the weak correlation limit.⁸ Thus even weak correlations may be sufficient to induce an insulating state. Overall, a correct understanding of the electronic structure is important for evaluating the relevance of localized spin-Hamiltonians such as the (extended) Heisenberg-Kitaev models currently under discussion for these materials. It is generally agreed that long-range second and/or third neighbour interactions are required to understand the magnetism in the 2D honeycomb Na₂IrO₃ and α -Li₂IrO₃²⁰, suggesting relatively delocalized moments.

Three-dimensional generalizations of the honeycomb lattices were also recently synthesized; the hyperhoneycomb β -Li₂IrO₃^{11,12} and the stripy honeycomb γ -Li₂IrO₃^{13,14} (Fig. 1). These materials are expected to display 3D Kitaev physics and to potentially support quantum spin liquid states analogous to the 2D case^{15–17}. Resonant magnetic x-ray diffraction experiments found that γ -Li₂IrO₃ hosts, at low temperatures, a non-coplanar counter-rotating long range spiral magnetic

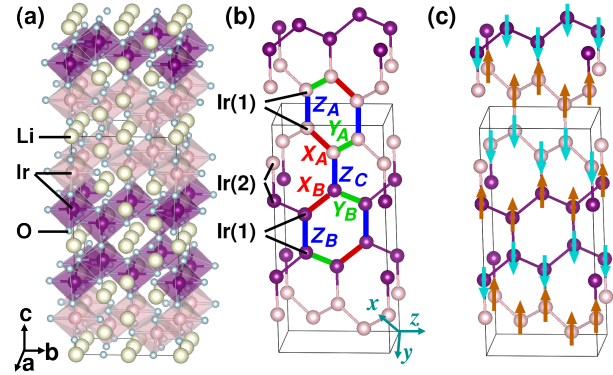


FIG. 1: (Color online) (a) Crystal structure of stripy honeycomb γ -Li₂IrO₃^{13,14}. Honeycomb rows alternate in orientation along c . The black axis a , b , and c are the vectors of the unit cell. (b) Crystal structure showing only Ir atoms. The red, green and blue bonds show the seven different types of bonds X_A , X_B , Y_A , Y_B , Z_A , Z_B , Z_C . x , y , z are the cartesian coordinates for the d orbitals. (c) Zigzag magnetic configuration used in our GGA+SO+U calculations.

order with incommensurate ordering wavevector $\mathbf{q} = (0.57, 0, 0)$ along the orthorhombic a -axis^{12,14}. Various investigations of the combined Kitaev-Heisenberg spin Hamiltonian suggest that Kitaev interactions must dominate over the Heisenberg terms in order to produce the observed complex spin spirals^{7,14,16–19}, although long-range antisymmetric interactions cannot be ignored²⁰.

In order to gain microscopic insight on the electronic properties of γ -Li₂IrO₃ in comparison to its 2D counterparts, we consider the electronic structure and optical conductivity of each material within density functional theory (DFT) and the exact diagonalization (ED) method. Optical conductivity measurements for γ -Li₂IrO₃²¹ show anisotropic behavior between polarizations along the a and b axes, but both polarizations show a broad peak structure at 1.5 eV, similar to that of Na₂IrO₃. However, the observed optical conductivity was significantly reduced in magnitude for γ -Li₂IrO₃ compared to Na₂IrO₃. This difference was initially attributed

TABLE I: Nearest neighbour distances (in Å) and Ir-O-Ir angles for the different bond types, determined in the experimental γ -Li₂IrO₃ structure (see Fig. 1 (b) for bond notation).

γ -Li ₂ IrO ₃	X_A, Y_A	Y_B, X_B	Z_A, Z_B	Z_C
Ir-Ir distance	2.976		2.982	2.96
Ir-O1 distance	1.99, 2.14		2.10	1.97
Ir-O2 distance	2.01, 2.01		2.10	1.97
Ir-O1-Ir angle	92.00°		90.37°	97.40°
Ir-O2-Ir angle	95.52°		90.37°	97.40°

to the inherently 3D versus 2D structure rather than the replacement of Na by Li²¹. This issue is addressed in Section III. The remaining paper is organized as follows. In section II, we discuss the electronic structure of γ -Li₂IrO₃ from the perspective of both DFT calculations and exact diagonalization of small clusters. In section III, we relate the electronic structure to the optical conductivity, including detailed discussion of the differences between DFT and ED results. Finally, in section IV we compare the results for γ -Li₂IrO₃ to the 2D honeycomb lattice analogues Na₂IrO₃ and α -Li₂IrO₃. In particular, in this last section, we present results based on the newly available single-crystal structure of α -Li₂IrO₃³⁷.

II. ELECTRONIC PROPERTIES OF γ -Li₂IrO₃

A. Crystal Structure

The experimental structure of γ -Li₂IrO₃^{13,14} (see Fig. 1 (a)-(b)) has two hexagonal chains oriented in the directions $a \pm b$ linked along the c -direction. There are three kinds of Z bonds in γ -Li₂IrO₃: the Z_C bond bridges two chains of hexagons while the Z_A and Z_B bonds complete each Ir hexagon in the layered structure. The cartesian coordinates x, y, z for the orbitals are displayed in Fig. 1 (b). The unit cell has two nonequivalent Ir atoms and a total of eight Ir: Ir(1) atoms are linked by Z_A and Z_B bonds, while Ir(2) atoms are linked by Z_C bonds. X_A, Y_A, X_B and Y_B link Ir(1) and Ir(2) sites. Details of the crystal structure are given in Table I.

B. Density Functional Theory Calculations

We performed linearized augmented plane-wave (LAPW) calculations²⁴ with the generalized gradient approximation (GGA)²⁵. We chose the basis-size controlling parameter $RK_{\max} = 8$ and a mesh of 432 \mathbf{k} points in the first Brillouin zone (FBZ) of the primitive unit cell. Relativistic effects were taken into account within the second variational approximation. A $U_{\text{eff}} = 2.4$ eV as implemented in GGA+SO+U²⁶ was employed in order to keep consistency with previous calculations¹⁰.

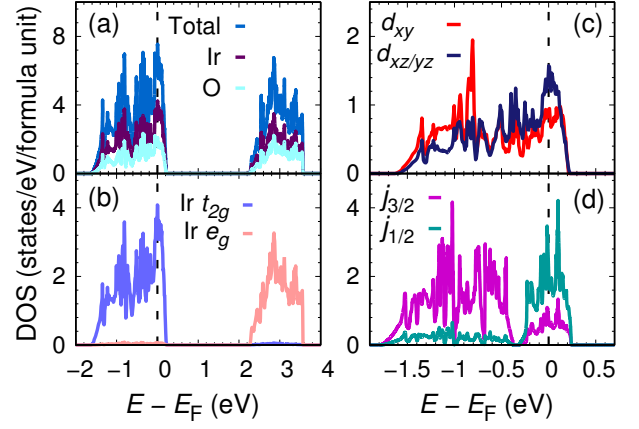


FIG. 2: (Color online) Density of states (DOS) for γ -Li₂IrO₃ in the nonmagnetic configuration obtained (a-c) within GGA and (d) GGA+SO.

The hopping parameters between Ir 5d orbitals in γ -Li₂IrO₃ were computed via the Wannier function projection method^{9,20,27,28} and we employed the optics code package²⁹ within LAPW to calculate the optical conductivity. The density of states and optical properties were computed with $10 \times 10 \times 10$ \mathbf{k} points in the full Brillouin zone while the hopping parameters were evaluated using $12 \times 12 \times 12$ \mathbf{k} points.

The non-relativistic GGA density of states (DOS) for γ -Li₂IrO₃ is displayed in Fig. 2 (a) - (c). The Iridium 5d states are split into e_g (2.2 eV to 3.6 eV) and t_{2g} (-1.6 eV to 0.2 eV) states (Fig. 2 (b)) due to the octahedral crystal field of IrO₆ with the Fermi level lying within the t_{2g} manifold. The t_{2g} band is further slightly split into lower d_{xy} and higher d_{xz}, d_{yz} (Fig. 2 (c)), arising from an additional weak trigonal field. By using the projection method described in Ref. 9, we obtained the hopping parameters from the GGA bandstructure. Table II displays the crystal field splitting compared with Na₂IrO₃. Full hopping integral tables are given in Appendix A. In terms of the t_{2g} d -orbital basis:

$$\vec{c}_i^\dagger = \left(c_{i,yz,\uparrow}^\dagger, c_{i,yz,\downarrow}^\dagger, c_{i,xz,\uparrow}^\dagger, c_{i,xz,\downarrow}^\dagger, c_{i,xy,\uparrow}^\dagger, c_{i,xy,\downarrow}^\dagger \right) \quad (1)$$

the crystal field terms can be written:

$$\mathcal{H}_{\text{CF}} = - \sum_i \vec{c}_i^\dagger \{ \mathbf{E}_i \otimes \mathbb{I}_{2 \times 2} \} \vec{c}_i \quad (2)$$

where $\mathbb{I}_{2 \times 2}$ is the 2×2 identity matrix (for the spin variables); the crystal field tensor \mathbf{E}_i is constrained by local 2-fold symmetry at each Ir site to be:

$$\mathbf{E}_i = \begin{pmatrix} 0 & \Delta_1 & \Delta_2 \\ \Delta_1 & 0 & \Delta_2 \\ \Delta_2 & \Delta_2 & \Delta_3 \end{pmatrix} \quad (3)$$

The t_{2g} crystal fields Δ_1, Δ_2 denote the on-site hopping between d_{xz} and d_{yz} orbitals, and between d_{xy} and $d_{yz/xz}$

TABLE II: Crystal field splitting compared with Na_2IrO_3 . The t_{2g} crystal fields Δ_1 , Δ_2 denote, respectively, the onsite hopping between d_{xz} and d_{yz} orbitals, d_{xy} and $d_{yz/xz}$ orbitals. Δ_3 is the on-site energy of d_{xy} minus $d_{yz/xz}$ ²⁰.

Crystal field	Na_2IrO_3 ²⁰	$\gamma\text{-Li}_2\text{IrO}_3$	
Parameter		Ir(1)	Ir(2)
Δ_1	-22.9	-24.4	-29.9
$ \Delta_2 $	27.6	4.2	37.4
Δ_3	-27.2	-213.5	-110.9

orbitals, respectively (Table II). Δ_3 is the on-site energy of d_{xy} minus that of $d_{yz/xz}$ ²⁰. Δ_3 is -213.5 meV for Ir(1) and -110.9 meV for Ir(2) (see Fig. 1), which is much larger in magnitude than in Na_2IrO_3 (-27.2 meV)²⁰. This means that in the 3D $\gamma\text{-Li}_2\text{IrO}_3$ structure, the t_{2g} crystal field is of the same order of magnitude as the spin-orbit coupling $\lambda \sim 400$ meV and this likely has significant effects on the local magnetic interactions.

Table III shows the nearest neighbour hopping parameters where $t_{1\parallel}$, t_{1O} and $t_{1\sigma}$ are defined as in Ref. 9 (labelled t_1 , t_2 , and t_3 in Ref. 6,20); t_{1O} (t_2) refers to effective Ir–Ir hopping through the bridging oxygens, $t_{1\sigma}$ (t_3) and $t_{1\parallel}$ (t_1) refer to σ - and δ -type direct metal-metal hopping, respectively. A full table of hopping integrals in the t_{2g} basis are given in the Appendix. There are three significant differences in the nearest neighbour hoppings of the 3D $\gamma\text{-Li}_2\text{IrO}_3$ (see Table III) when compared with Na_2IrO_3 : i) the direct metal-metal hopping t_3 ($d_{xy} \rightarrow d_{xy}$) along the Z_A and Z_B bonds (Fig. 1 (b)) is larger than the oxygen-assisted hopping t_2 ($d_{xz} \rightarrow d_{yz}$, $d_{yz} \rightarrow d_{xz}$) due to the nearly 90° Ir–O–Ir angle (Table I). ii) the t_2 in the X_A (Y_A), X_B (Y_B) bonds have opposite signs, as a result of different local environments (see Appendix). The different sign arises because such bonds are related to one another by crystallographic 2-fold rotations. Finally, iii) the absence of inversion symmetry for the majority of nearest neighbour bonds allows for some asymmetry in the t_2 hopping, e.g. for the X_A bond, $d_{xy} \rightarrow d_{xz}$ and $d_{xz} \rightarrow d_{xy}$ hoppings are unequal. For this reason, a finite Dzyaloshinskii-Moriya (DM) interaction is both allowed and expected to appear for the majority of first-neighbour bonds: X_A , X_B , Y_A , Y_B , and Z_C . This result is in contrast to Na_2IrO_3 and $\alpha\text{-Li}_2\text{IrO}_3$, for which a weaker DM interaction only exists for the second nearest neighbour bonds²⁰. Since these antisymmetric interactions are likely to strongly stabilize the observed incommensurate magnetic order¹⁴, one may question the completeness of previous interaction models for $\gamma\text{-Li}_2\text{IrO}_3$ including only symmetric exchange interactions^{16,18}.

Unlike the 2D Na_2IrO_3 , the 3D $\gamma\text{-Li}_2\text{IrO}_3$ does not allow a clear description of the DFT electronic structure in terms of QMOs. Indeed, there is no pseudogap at the Fermi energy at the GGA+SO level (Fig. 2(d)), in contrast with Na_2IrO_3 . As in the $P3_12$ structure of

TABLE III: Nearest neighbour hopping integrals in meV between Ir t_{2g} orbitals for the experimental $\gamma\text{-Li}_2\text{IrO}_3$ structure (see Fig. 1 (b) for bond notation). The labels $t_{1\parallel}$, t_{1O} and $t_{1\sigma}$ are the same as in Ref. 9, and the notations t_1 , t_2 and t_3 are given in Ref. 6,20.

$\gamma\text{-Li}_2\text{IrO}_3$	X_A, Y_A	Y_B, X_B	Z_A, Z_B	Z_C
$t_{1\parallel}$ (t_1)	91.4	91.4	91.8	77.4
	69.2	69.2	91.8	77.4
t_{1O} (t_2)	-262.5	262.5	132.8	294.1
	-240.5	240.5	132.8	294.1
$t_{1\sigma}$ (t_3)	-168.3	-168.3	-319.7	-17.1

$\alpha\text{-RuCl}_3$ ³¹, the oxygen assisted hopping t_{1O} , which is crucial for the formation of the QMOs, is smaller than $t_{1\sigma}$ ^{9,31}. In addition, since not all local Ir 5d orbitals can be attributed to a single hexagon, the QMO basis is incomplete. We therefore choose to work with the j_{eff} basis. Fig. 2 (d) shows the projection of the GGA+SO DOS onto the j_{eff} basis. At the Fermi level, the DOS is dominantly $j_{\text{eff}} = 1/2$ with a small contribution from $j_{\text{eff}} = 3/2$.

According to experiment, the magnetic ground state in $\gamma\text{-Li}_2\text{IrO}_3$ is spin spiral¹⁴ and the magnetic structure shows that the zigzag chains in the a direction are connected along the c direction (see Fig. 1 (c)). In order to perform spin-polarized DFT calculations in the magnetically ordered state, we employed a collinear zigzag magnetic configuration with spin polarization along the c direction as an approximate representation of the ordered configuration¹⁴. Calculations with the spin polarization along a are shown in Appendix B for comparison. Inclusion of U within the GGA+SO+ U approach in the zigzag magnetic configuration (Fig. 1(c)) opens a gap of 242 meV (Fig. 3) which is smaller than the experimentally measured value of 0.5 eV²¹. We note that the size of the gap is influenced by the choice of U . We however decided here to use the same U parameter as for previous calculations for Na_2IrO_3 and $\alpha\text{-Li}_2\text{IrO}_3$ ¹⁰ in order to allow a better comparison below. The magnetic moment converged to 0.58 μ_B for Ir(1) and 0.44 μ_B for Ir(2).

C. Exact Diagonalization of Finite Clusters

While the GGA+SO+ U calculations are able to describe many significant aspects of the electronic structure of $\gamma\text{-Li}_2\text{IrO}_3$ they do not fully capture effects originating from correlations beyond GGA+SO+ U , which are expected to be relevant when analyzing electronic excitations. Therefore, we consider here a complementary approach to DFT, namely exact diagonalization of the fully interacting Hamiltonian on finite clusters³² and compare with DFT results.

We have employed four-site clusters shown in the inset of Fig. 5 and obtained the exact eigenstates of the Ir

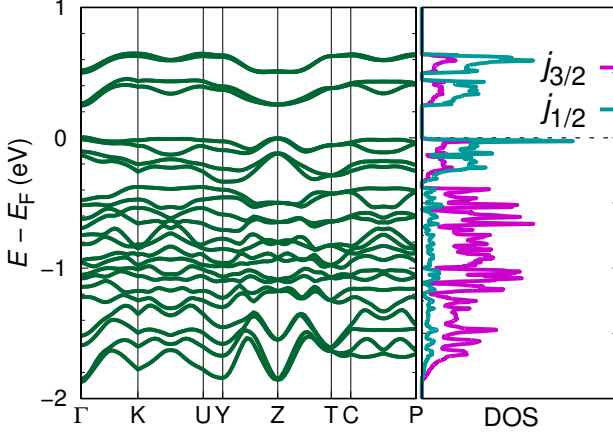


FIG. 3: (Color online) Ir 5d t_{2g} band structure and relativistic DOS for γ -Li₂IrO₃ in zigzag magnetic order, obtained with GGA+SO+U ($U_{\text{eff}} = U - J_{\text{H}} = 2.4$ eV).

t_{2g} -only Hamiltonian described in Ref. 20:

$$\mathcal{H}_{\text{tot}} = \mathcal{H}_{\text{hop}} + \mathcal{H}_{\text{CF}} + \mathcal{H}_{\text{SO}} + \mathcal{H}_U \quad (4)$$

including the kinetic hopping term \mathcal{H}_{hop} , the crystal field splitting \mathcal{H}_{CF} , spin-orbit coupling \mathcal{H}_{SO} , and Coulomb interaction \mathcal{H}_U . In terms of the t_{2g} basis introduced above, spin-orbit coupling (SOC) is described by:

$$\mathcal{H}_{\text{SO}} = \frac{\lambda}{2} \sum_i \vec{c}_i^\dagger \begin{pmatrix} 0 & -i\sigma_z & i\sigma_y \\ i\sigma_z & 0 & -i\sigma_x \\ -i\sigma_y & i\sigma_x & 0 \end{pmatrix} \vec{c}_i \quad (5)$$

where σ_μ , $\mu = \{x, y, z\}$ are Pauli matrices. The Coulomb terms are:

$$\begin{aligned} \mathcal{H}_U = & U \sum_{i,a} n_{i,a,\uparrow} n_{i,a,\downarrow} + (U' - J_{\text{H}}) \sum_{i,a < b, \sigma} n_{i,a,\sigma} n_{i,b,\sigma} \\ & + U' \sum_{i,a \neq b} n_{i,a,\uparrow} n_{i,b,\downarrow} - J_{\text{H}} \sum_{i,a \neq b} c_{i,a,\uparrow}^\dagger c_{i,a,\downarrow} c_{i,b,\downarrow}^\dagger c_{i,b,\uparrow} \\ & + J_{\text{H}} \sum_{i,a \neq b} c_{i,a,\uparrow}^\dagger c_{i,a,\downarrow}^\dagger c_{i,b,\downarrow} c_{i,b,\uparrow} \end{aligned} \quad (6)$$

where $c_{i,a}^\dagger$ creates a hole in orbital $a \in \{d_{yz}, d_{xz}, d_{xy}\}$ at site i ; J_{H} gives the strength of Hund's coupling, U is the *intraorbital* Coulomb repulsion, and $U' = U - 2J_{\text{H}}$ is the *interorbital* repulsion. For 5d Ir⁴⁺, we take $U = 1.7$ eV, $J_{\text{H}} = 0.3$ eV⁴. For the four-site clusters, we retain all hoppings including second neighbour.

For γ -Li₂IrO₃, there are four translationally inequivalent clusters constructed from bonds (X_A, Y_A, Z_A) , (X_B, Y_B, Z_B) , (X_A, Y_A, Z_C) , and (X_B, Y_B, Z_C) . Of these, the first two are related to one another by 2-fold rotation and the last two are also related by 2-fold rotation. The results presented correspond to an average over these four clusters. In each four-site cluster, we consider states with a total of four holes in the t_{2g} orbitals; each Ir site

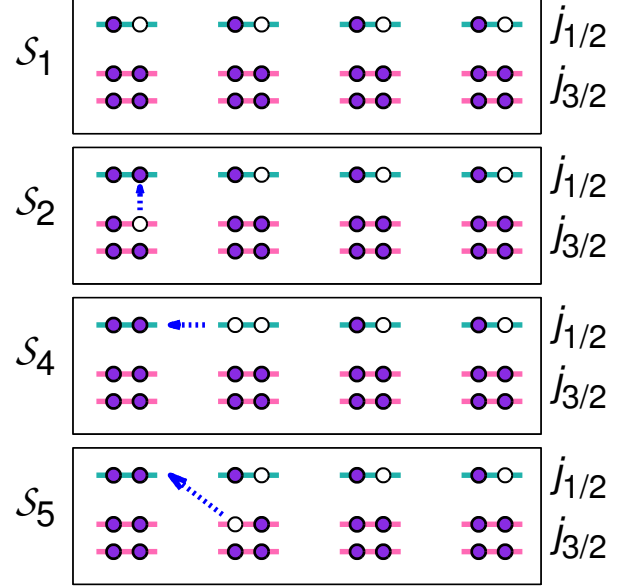


FIG. 4: (Color online) Schematic diagrams of lowest energy subspace \mathcal{S}_1 and one particle excitations \mathcal{S}_2 , \mathcal{S}_4 , and \mathcal{S}_5 . Solid circles indicate electrons while empty circles are holes. \mathcal{S}_1 are all the states with $(j_{3/2})^4(j_{1/2})^1$, \mathcal{S}_2 are the states obtained from \mathcal{S}_1 by promoting an electron $j_{3/2} \rightarrow j_{1/2}$ on the same site. \mathcal{S}_4 are the states obtained from \mathcal{S}_1 by promoting an *intersite* $j_{1/2} \rightarrow j_{1/2}$ transition, and \mathcal{S}_5 are the states with promotion of an electron $j_{3/2} \rightarrow j_{1/2}$.

contains six relativistic orbitals including two $j_{\text{eff}} = 1/2$ and four $j_{\text{eff}} = 3/2$ levels. As in Ref. 32, the many-body basis states for the cluster can be divided into several subspaces based on the occupancy of the various orbitals and sites. Basis states with site occupancy $d^5 - d^5 - d^5 - d^5$ are included in subspaces $\mathcal{S}_1 - \mathcal{S}_3$, states with site occupancy $d^4 - d^6 - d^5 - d^5$ belong to $\mathcal{S}_4 - \mathcal{S}_7$, and \mathcal{S}_8 contains all higher excitations. We show representative diagrams of the lowest energy subspace \mathcal{S}_1 and one particle excitation \mathcal{S}_2 , \mathcal{S}_4 , and \mathcal{S}_5 in Fig. 4. Subspace \mathcal{S}_1 contains all states with $(j_{3/2})^4(j_{1/2})^1$ occupancy at every site, which represent a significant contribution to the ground state and low-lying magnon-like spin excitations.

From these configurations, promotion of a single electron via *onsite* $j_{3/2} \rightarrow j_{1/2}$ generates subspace \mathcal{S}_2 , containing all states with a single spin-orbital exciton; the characteristic excitation energy for such states is given by $\Delta E_2 \sim 3\lambda/2 \sim 0.6$ eV. All states with multiple excitons are grouped into subspace \mathcal{S}_3 , and represent n -particle excitations from the ground state, with energies $\Delta E_3 \sim 3n\lambda/2 \sim 1.2, 1.8, \dots$ eV.

Starting from \mathcal{S}_1 , promotion of an electron via *intersite* $j_{1/2} \rightarrow j_{1/2}$ yields subspace \mathcal{S}_4 , containing states with

characteristic energy $\Delta E_4 \sim \mathbb{A}^{-1}$, where²⁰:

$$\mathbb{A} = -\frac{1}{3} \left\{ \frac{J_H + 3(U + 3\lambda)}{6J_H^2 - U(U + 3\lambda) + J_H(U + 4\lambda)} \right\} \quad (7)$$

Taking $U = 1.7$ eV, $J_H = 0.3$ eV, and $\lambda = 0.4$ eV suggests $\Delta E_4 \sim 1.1$ eV.

Starting from \mathcal{S}_1 , promotion of an electron via *intersite* $j_{3/2} \rightarrow j_{1/2}$ yields subspace \mathcal{S}_5 , containing states with characteristic energy $\Delta E_5 \sim \mathbb{C}^{-1} \sim 1.6$ eV, where²⁰:

$$\mathbb{C} = \frac{6}{8} \left\{ \frac{1}{2U - 6J_H + 3\lambda} + \frac{5(3U - 7J_H + 9\lambda)}{9J_H} \eta \right\} \quad (8)$$

$$\eta = \frac{J_H}{6J_H^2 - J_H(8U + 17\lambda) + (2U + 3\lambda)(U + 3\lambda)} \quad (9)$$

Subspace \mathcal{S}_6 contains two-particle excited states for which the d^4 site contains occupancies $(j_{3/2})^2(j_{1/2})^2$, while subspace \mathcal{S}_7 contains all other excitations with occupancy of $d^4 - d^6 - d^5 - d^5$. Single particle excitations most relevant for the optical conductivity in the next section are contained in $\mathcal{S}_1, \mathcal{S}_4, \mathcal{S}_5$. The effect of intersite hopping (and Hund's coupling) is to mix states from different subspaces, but the characteristic energies remain valid.

In order to show this, we project the exact cluster eigenstates ϕ_m on different subspaces:

$$\Gamma_i^m = \sum_{s \in \mathcal{S}_i} |\langle \phi_m | s \rangle|^2, \quad (10)$$

and take the spectral weight (SW) of the projected excitation spectra P_i ³³:

$$P_i(\omega) = \sum_m \Gamma_i^m \delta(\omega - E_m). \quad (11)$$

P_1 to P_7 are shown in Fig. 5. As expected, the ground state and low-lying magnon-like spin excitations ($\omega \sim 0$ eV) have the dominant \mathcal{S}_1 character (large P_1), while intersite hopping perturbatively mixes in some $\mathcal{S}_2, \mathcal{S}_4, \mathcal{S}_5$ character. Indeed, from the localized picture, it is the *intersite* $j_{3/2} \rightarrow j_{1/2}$ mixing that is the origin of the anisotropic Kitaev exchange couplings.

Regarding the higher excitations: centered at $\omega = \Delta E_2 \sim 0.6$ eV are the single exciton-like states, with dominant \mathcal{S}_2 character. These states weakly mix with the single-particle \mathcal{S}_4 and \mathcal{S}_5 and multi-particle \mathcal{S}_6 and \mathcal{S}_7 excitations via intersite hopping. As expected, excitations with dominant \mathcal{S}_4 character (i.e. $j_{1/2} \rightarrow j_{1/2}$) are centered around $\omega = \Delta E_4 \sim 1.1$ eV, and excitations with dominant \mathcal{S}_5 character (i.e. $j_{3/2} \rightarrow j_{1/2}$) are centered around $\omega = \Delta E_5 \sim 1.6$ eV. The widths of these bands are approximately 1 eV and 2 eV, respectively, which is consistent with the GGA+SO+U results above. It is worth noting that the total spectral weight $\int P_i d\omega$ is much larger for \mathcal{S}_5 than \mathcal{S}_4 , such that $j_{3/2} \rightarrow j_{1/2}$ excitations dominate the projected excitation spectra. Similar results were obtained in Ref. 32 in the analysis of the excitation spectrum of Na_2IrO_3 .

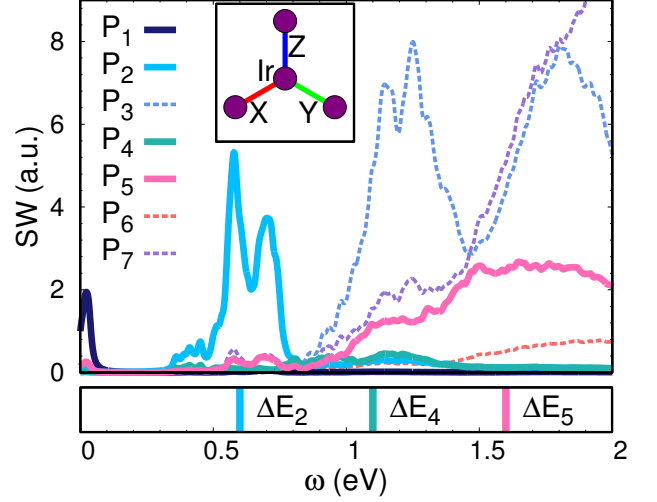


FIG. 5: (Color online) The investigated four-site cluster (inset) and spectral weight (SW) of projected excitations spectra for $\gamma\text{-Li}_2\text{IrO}_3$. P_1 includes all states with $(j_{3/2})^4(j_{1/2})^1$ (\mathcal{S}_1), P_2 and P_3 include the states with an exciton on one site (\mathcal{S}_2) or on more sites (\mathcal{S}_3), respectively. P_4 includes states from \mathcal{S}_1 with promotion of an electron $j_{1/2} \rightarrow j_{1/2}$ to another site (\mathcal{S}_4), and P_5 includes states with promotion of an electron $j_{3/2} \rightarrow j_{1/2}$ to another site (\mathcal{S}_5). P_6 is for states that contain two-particle excited states for which the d^4 site contains occupancies $(j_{3/2})^2(j_{1/2})^2$ (\mathcal{S}_6), while P_7 includes all other excitations with occupancy of $d^4 - d^6 - d^5 - d^5$ (\mathcal{S}_7). $\Delta E_2 \sim 0.6$ eV, $\Delta E_4 \sim 1.1$ eV, $\Delta E_5 \sim 1.6$ eV are the excitation energies for P_2, P_4 and P_5 respectively.

III. OPTICAL CONDUCTIVITY

We employ two methods to compute the optical conductivity. The interband contribution to the real part of the optical conductivity in the DFT calculations is approximated by^{29,30}:

$$\sigma_{\mu\nu}(\omega) \propto \frac{1}{\omega} \sum_{c,v} \int d\mathbf{k} \langle c_{\mathbf{k}} | p^\mu | v_{\mathbf{k}} \rangle \langle v_{\mathbf{k}} | p^\nu | c_{\mathbf{k}} \rangle \times \delta(\varepsilon_{c\mathbf{k}} - \varepsilon_{v\mathbf{k}} - \omega). \quad (12)$$

where μ and ν correspond to the cartesian axes x', y', z' , which is chosen as the direction of a, b, c in this system. ω indicates the energy of the incident photon, and p is the momentum operator. The states $|c_{\mathbf{k}}\rangle$ in \mathbf{k} space with energy $\varepsilon_{c\mathbf{k}}$ belong to occupied single-particle states, while $|v_{\mathbf{k}}\rangle, \varepsilon_{v\mathbf{k}}$ describe unoccupied states.

For the exact diagonalization calculations, we calculate the real part of the optical conductivity at finite temperature using³³

$$\sigma_{\mu\nu}(\omega) \propto \frac{\pi(1 - e^{-\omega/(k_B T)})}{\omega V} \sum_{nm} B_n M_{\mu,\nu}^{m,n} \delta(\omega + E_n - E_m) \quad (13)$$

where V is the volume, B_n is the probability density of eigenstate $|\phi_n\rangle$.

$$B_n = \frac{e^{-\beta E_n}}{\sum_{n'} e^{-\beta E_{n'}}} \quad (14)$$

and $M_{\mu,\nu}^{m,n}$ are matrix elements of the current operator:

$$M_{\mu,\nu}^{m,n} = \langle n | j_\mu | m \rangle \langle m | j_\nu | n \rangle \quad (15)$$

The current operator j_μ is given by³⁴:

$$j_\mu = \frac{ie}{\hbar} \sum_{\substack{i < j \\ a,b,\sigma,\sigma'}} (c_{i,a,\sigma}^\dagger c_{j,b,\sigma'} - c_{j,b,\sigma'}^\dagger c_{i,a,\sigma}) t_{i,j}^{a,b} \mathbf{r}_{ij}^\mu, \quad (16)$$

where $t_{i,j}^{a,b}$ are the hopping parameters between the t_{2g} orbitals and \mathbf{r}_{ij}^μ is the μ component of the vector from site j to site i . Note that the expression of the optical conductivity considered in Eq. (12) is defined at zero temperature and in k space while in Eq. (13) we consider the definition in real space and at finite temperature $k_B T = 30$ meV (room temperature). We observe that the finite temperature modifies the zero temperature results only slightly. The optical conductivity is normalized by the sum-rule that the energy integral of the optical conductivity in both ED and DFT methods is proportional to the effective density of electrons.

For γ -Li₂IrO₃, the orthorhombic symmetry of the space group allows the optical conductivity tensor to be defined in terms of the three independent components σ_a , σ_b , σ_c ($\sigma_a = \sigma_{x'x'}$, $\sigma_b = \sigma_{y'y'}$, $\sigma_c = \sigma_{z'z'}$):

$$\begin{pmatrix} J_a \\ J_b \\ J_c \end{pmatrix} = \begin{pmatrix} \sigma_a & 0 & 0 \\ 0 & \sigma_b & 0 \\ 0 & 0 & \sigma_c \end{pmatrix} \begin{pmatrix} E_a \\ E_b \\ E_c \end{pmatrix}. \quad (17)$$

In Fig. 6, we compare the DFT (GGA+U+SO), ED and experimental optical conductivity tensor components for γ -Li₂IrO₃. Both DFT and ED capture correctly the anisotropy $\sigma_a < \sigma_b < \sigma_c$, which is due to the structural orientation of the planes shown in the inset of Fig. 6 (b). Given that interplane hopping is very weak, the in-plane component of $\sigma(\omega)$ dominates. The magnitude of $\sigma(\omega)$ for polarization along each axis is therefore related to the projection of that axis on to the Ir planes. For light polarized along the c -axis, the response is solely due to in-plane processes, while polarization along the a - or b -axes measures only a fraction of the in-plane response. This observation explains the reduction of the measured $\sigma(\omega)$ (σ_a, σ_b) for γ -Li₂IrO₃ discussed in Ref. 21, when compared with the in-plane measurements of Na₂IrO₃.

While ED calculations show a dominant peak around $\omega = 1.6$ eV for all polarizations, consistent with the experimental data, the DFT results suggest also significant spectral weight at lower frequencies. The origin of this anomalous spectral weight can be found in Fig. 7. For

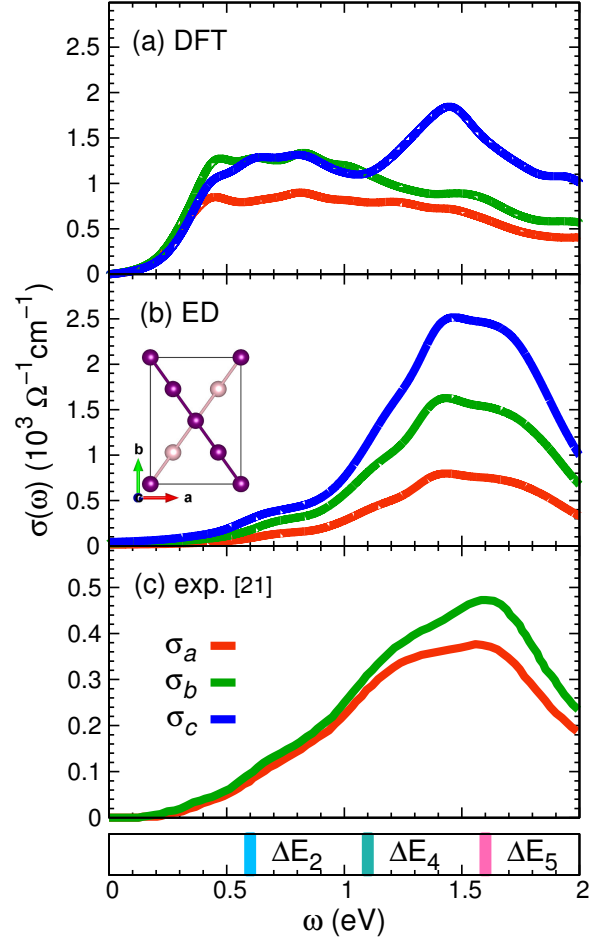


FIG. 6: (Color online) Optical conductivity components for γ -Li₂IrO₃. (a) Results from DFT within GGA+U+SO. (b) Results from exact diagonalization and (c) results reported from experimental observations²¹. $\Delta E_2 \sim 0.6$ eV, $\Delta E_4 \sim 1.1$ eV, $\Delta E_5 \sim 1.6$ eV are the characteristic excitation energy for subspaces \mathcal{S}_2 , \mathcal{S}_4 and \mathcal{S}_5 respectively. The inset of (b) is the crystal structure projected in the ab -plane.

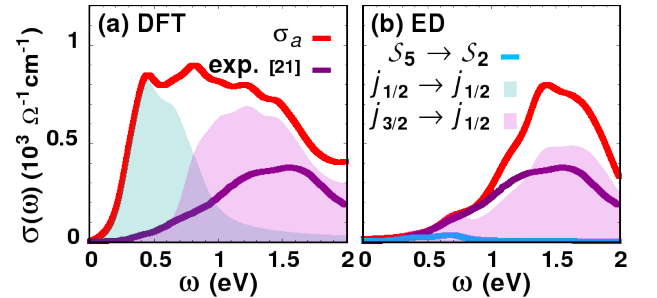


FIG. 7: (Color online) Optical conductivity component σ_a for γ -Li₂IrO₃ and different d - d transitions in the relativistic basis calculated (a) with DFT within GGA+U+SO and (b) with the ED method. The comparison to experiment is also shown²¹.

the DFT calculations, we show the decomposition of $\sigma(\omega)$ into intraband $j_{1/2} \rightarrow j_{1/2}$ and interband $j_{3/2} \rightarrow j_{1/2}$ excitations. For the ED calculations, we plot the projection of $\sigma(\omega)$ onto the $\mathcal{S}_1 \rightarrow \mathcal{S}_2$ (i.e. spin-orbital excitons), $\mathcal{S}_1 \rightarrow \mathcal{S}_4$ (i.e. $j_{1/2} \rightarrow j_{1/2}$), and $\mathcal{S}_1 \rightarrow \mathcal{S}_5$ (i.e. $j_{3/2} \rightarrow j_{1/2}$) excitations. Although direct $\mathcal{S}_1 \rightarrow \mathcal{S}_2$ excitations are optically forbidden, the spin-orbital excitonic states \mathcal{S}_2 also make a weak contribution to $\sigma(\omega)$ in the mid-energy range due to weak higher order effects. These contributions are also shown. Both the DFT and ED calculations suggest that the peak around 1.6 eV is due primarily to interband $j_{3/2} \rightarrow j_{1/2}$ contributions. The anomalous low-frequency ($\omega < 1$ eV) spectral weight in the DFT arises primarily from $j_{1/2} \rightarrow j_{1/2}$ excitations between the upper and lower Hubbard bands, the intensity of which are dramatically suppressed in the ED results. This difference can be traced back to two main effects:

(i) From a localized perspective, we can consider the ground state for two sites as having an electronic configuration \mathcal{S}_1 : site 1 = $(j_{3/2})^4(j_{1/2})^1$, site 2 = $(j_{3/2})^4(j_{1/2})^1$. Intersite $j_{1/2} \rightarrow j_{1/2}$ transitions yield local configurations like \mathcal{S}_4 : $(j_{3/2})^4(j_{1/2})^0 - (j_{3/2})^4(j_{1/2})^2$, which have a low spin degeneracy as a result of the filled or empty $j_{1/2}$ states. Intersite $j_{3/2} \rightarrow j_{1/2}$ excitations yield local configurations like \mathcal{S}_5 : $(j_{3/2})^3(j_{1/2})^1 - (j_{3/2})^4(j_{1/2})^2$, which have a larger spin-degeneracy due to the partially filled $j_{3/2}$ and $j_{1/2}$ states. Overall, the ratio of the total spectral weight associated with these transitions should be $\int P_4(\omega) : \int P_5(\omega) = 1 : 8$, as shown in Fig. 5. In contrast, the DFT calculations take an effective single-particle momentum space perspective, in which the $j_{3/2}$ band is fully occupied, and the $j_{1/2}$ band is half-occupied. The spectral weight associated with $j_{1/2} \rightarrow j_{1/2}$ and $j_{3/2} \rightarrow j_{1/2}$ transitions is therefore 1 : 4, which overestimates the contributions of the former in DFT calculations compared to the localized picture. In other words, DFT does not correctly capture the spin-multiplicity associated with the localized states.

(ii) In a localized picture, the current operator depends on the intersite hopping matrix elements via Eq. (16). It is therefore useful to rewrite the nearest neighbour hopping integrals in the relativistic basis. For example, for the Z-bonds, these are:

$$t_{ij}(j_{1/2} \rightarrow j_{1/2}) \propto (2t_1 + t_3) \quad (18)$$

$$t_{ij}(j_{3/2}; m_{\pm 1/2} \rightarrow j_{1/2}) \propto (t_3 - t_1) \quad (19)$$

$$t_{ij}(j_{3/2}; m_{\pm 3/2} \rightarrow j_{1/2}) \propto t_2 \quad (20)$$

Via the current operator Eqs. (15)-(16), the optical conductivity associated with each transition scales with $\sigma(\omega) \propto (t_{ij})^2$. Typically, in the corner-sharing iridates such as γ -Li₂IrO₃, t_1 and t_3 have opposite sign (and may be quite small), which suppresses the $(j_{1/2} \rightarrow j_{1/2})$ hopping, reducing the influence of such excitations on the optical conductivity. This effect is partially captured in DFT, as can be seen from comparing the relative widths of the $j_{1/2}$ and $j_{3/2}$ bands in Fig. 3. However, DFT likely overestimates the degree of $j_{1/2} - j_{3/2}$ mixing which leads,

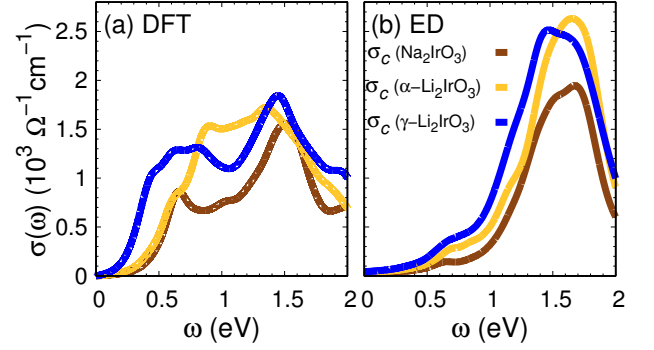


FIG. 8: (Color online) Optical conductivity σ_c for Na₂IrO₃, α -Li₂IrO₃, and γ -Li₂IrO₃ calculated (a) with DFT within GGA+U+SO and (b) with the ED method. σ_c for Na₂IrO₃ and α -Li₂IrO₃ corresponds to σ_{zz} in Ref. 10. Please note that for α -Li₂IrO₃ differences in the DFT optical conductivity with respect to results in Ref. 10 lie in the employed crystal structure.

effectively, to larger optical matrix elements between low-energy states.

Overall, we conclude that the ED calculations, based on DFT hopping integrals, provides the best description of the optical conductivity.

IV. COMPARISON TO Na₂IrO₃ AND α -Li₂IrO₃

Despite differences in crystal architecture, the experimental optical conductivity of γ -Li₂IrO₃ and Na₂IrO₃ share a very similar profile that we will analyze in what follows. As stated in the previous section, $\sigma(\omega)$ should be dominated by intersite $j_{3/2} \rightarrow j_{1/2}$ excitations, at $\omega \sim \mathbb{C}^{-1} \sim 1.6$ eV, as observed. The soft shoulder observed at lower energies results from a combination of low spectral weight from intersite $j_{1/2} \rightarrow j_{1/2}$ excitations centered at $\omega \sim \mathbb{A}^{-1} \sim 1.1$ eV, and weak mixing with optically forbidden local $j_{3/2} \rightarrow j_{1/2}$ excitons near $\omega \sim 0.6$ eV. These assignments are consistent with the fitting of $\sigma(\omega)$ in Ref. 35 for Na₂IrO₃, which suggested peaks in the vicinity of 0.72, 1.32, and 1.66 eV. However, the “band gap” reported to be 0.32 eV is likely to be significantly contaminated by low-lying excitonic states, and may therefore not represent the natural charge gap of the material. The origin of the peaks for Na₂IrO₃ in the relativistic basis are shown in Fig. 9 for both calculations.

In Fig. 8 we display the theoretical DFT and ED results for the in-plane σ_c component for Na₂IrO₃, α -Li₂IrO₃ and γ -Li₂IrO₃. For α -Li₂IrO₃, we employed the recently obtained single crystal structure³⁷. Hopping integrals and crystal field parameters for the revised structure are given in the Appendix. It should be noted that the results obtained for α -Li₂IrO₃ in this work therefore differ slightly from the results in Ref. 10, which employed instead previously available structures obtained from pow-

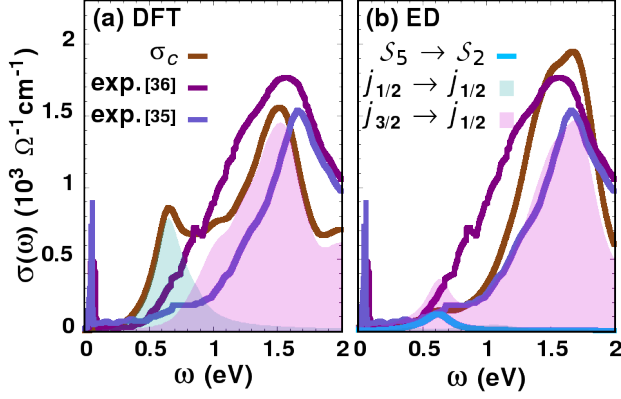


FIG. 9: (Color online) Optical conductivity component σ_c for Na_2IrO_3 and different d - d transitions in the relativistic basis calculated (a) with DFT within GGA+U+SO and (b) with the ED method. Comparison with experimental results from Ref. 36 and Ref. 35 is also shown. σ_c of Na_2IrO_3 corresponds to the σ_{zz} component in Ref. 10.

der x-ray analysis and structural relaxation. Generally for these materials, the electronic structure is strongly affected by the competition between spin-orbit coupling ($\lambda \sim 0.4$ eV) and crystal-field terms ($\Delta_n \sim 0 - 0.2$ eV), which leads to an enhanced dependence of the spectra on structural details. Nonetheless, both DFT and ED calculations give a strong main peak in $\sigma(\omega)$ near $\omega = 1.6$ eV for $\alpha\text{-Li}_2\text{IrO}_3$, $\gamma\text{-Li}_2\text{IrO}_3$ and Na_2IrO_3 . This peak is predicted to be more intense in the former two materials by both methods. Further, both DFT and ED calculations show an enhanced spectral weight at lower energies in $\gamma\text{-Li}_2\text{IrO}_3$ with respect to Na_2IrO_3 , which is consistent with experimental results. The differences can be understood as follows. For materials dominated by oxygen-assisted hopping such as Na_2IrO_3 , the hopping integrals in the d -orbital basis satisfy $t_2 \gg t_1, t_3$, so in the relativistic basis the hopping is dominated by $t_{ij}(j_{3/2}; m_{\pm 3/2} \rightarrow j_{1/2})$. This observation suggests negligible spectral weight for $j_{1/2} \rightarrow j_{1/2}$ excitations in $\sigma(\omega)$. In contrast, for significant direct metal-metal hopping t_1, t_3 , additional spectral weight may appear in the mid-energy region due to enhanced $t_{ij}(j_{1/2} \rightarrow j_{1/2})$. This is worth noting because the values of these hopping integrals are directly related to the magnetic interactions. Indeed, up to second order in hopping, the magnetic interactions are given by:²⁰

$$J_1 = \frac{4\mathbb{A}}{9}(2t_1 + t_3)^2 - \frac{8\mathbb{B}}{9}\{2(t_1 - t_3)^2\} \quad (21)$$

$$K_1 = \frac{8\mathbb{B}}{3}\{(t_1 - t_3)^2 - 3t_2^2\} \quad (22)$$

$$\Gamma_1 = \frac{8\mathbb{B}}{3}\{2t_2(t_1 - t_3)\} \quad (23)$$

where \mathbb{B} is a constant similar to \mathbb{A} and \mathbb{C} :

$$\mathbb{B} = \frac{4}{3} \left\{ \frac{(3J_H - U - 3\lambda)}{(6J_H - 2U - 3\lambda)} \eta \right\} \quad (24)$$

The desirable Kitaev limit ($K_1 \gg J_1, \Gamma_1$) is obtained only for $t_2 \gg t_1, t_3$, and will therefore be most closely approached by materials with the low spectral weight near $\omega \sim 1.1$ eV. This identifies Na_2IrO_3 as the closest material to the Kitaev limit from all three investigated here, in agreement with Ref. 20.

V. SUMMARY

We have investigated the electronic structure, hopping parameters and optical excitation spectrum of the three-dimensional $\gamma\text{-Li}_2\text{IrO}_3$. Due to the lower symmetry of the local Ir-O-Ir environment, the hopping integrals display significant deviations from the ideal case, suggesting e.g. large metal-metal hoppings and departures from inversion symmetric values. This situation likely leads to highly complex magnetic interactions in this system and manifests in certain signatures in the optical conductivity.

We computed the optical conductivity by two methods; (i) relativistic DFT calculations within GGA+SO+U and (ii) exact diagonalization of the full interacting Hamiltonian on finite clusters where the hopping integrals were obtained from DFT. Both methods reproduce the main peak of the in-plane component of the optical conductivity σ_c . However, GGA+SO+U seems to overestimate the contribution of the $j_{1/2} \rightarrow j_{1/2}$ transition at low energies in σ_a and σ_b . The ED results, in contrast, validate the model parameters (U, J_H, λ) and suggest that the high-lying excitations appear to be well captured within a localized picture in $\gamma\text{-Li}_2\text{IrO}_3$. The comparison with the optical conductivity analysis of Na_2IrO_3 shows that the peak near 1.5 eV in both Na_2IrO_3 and $\gamma\text{-Li}_2\text{IrO}_3$ can be identified in terms of *intersite* $j_{3/2} \rightarrow j_{1/2}$ excitations. The comparison of $\sigma(\omega)$ for the various materials suggests that the relative spectral weight of the transitions provide insight into the magnitudes of various hopping integrals, and therefore the local magnetic interactions.

Acknowledgments

We would like to thank Daniel Guterding and Kira Riedl for very useful discussions. We would also like to thank Philipp Gegenwart for pointing out the new single crystal structural data of $\alpha\text{-Li}_2\text{IrO}_3$. Y.L. acknowledges support through a China Scholarship Council (CSC) Fellowship. S. M. W. acknowledges support through an NSERC Canada Postdoctoral Fellowship. H.O.J and R.V. acknowledge support by the Deutsche Forschungsgemeinschaft through grant SFB/TR 49.

Appendix A: Hopping parameters for the nonmagnetic nonrelativistic system

Table IV and Table V show all onsite and nearest neighbor hopping parameters in γ -Li₂IrO₃. As noted above, the t_{1O} in the X_A (Y_A), X_B (Y_B) bonds have opposite signs, as a result of different local environments. The negative value corresponds to type 1 bonds in Fig. 10, while the positive values are type 2 bonds in Fig. 10.

Table VI and Table VII show all onsite and nearest neighbor hopping parameters in α -Li₂IrO₃.

TABLE IV: Hopping parameters for the on-site terms (meV) in γ -Li₂IrO₃. A is for hexagon including X_A , Y_A , Z_A bonds while B is for hexagon including X_B , Y_B , Z_B .

Ir(1)	$xy \rightarrow xy$	-592.6
	$xz \rightarrow xz$	-379.1
	$yz \rightarrow yz$	-379.1
Ir(2)	$xy \rightarrow xy$	-651.3
	$xz \rightarrow xz$	-540.4
	$yz \rightarrow yz$	-540.4
Ir(1)	$xy \rightarrow xz$	4.2 (A), -4.2 (B)
	$xy \rightarrow yz$	4.2 (A), -4.2 (B)
	$xz \rightarrow yz$	-24.4
Ir(2)	$xy \rightarrow xz$	37.4 (A), -37.4 (B)
	$xy \rightarrow yz$	37.4 (A), -37.4 (B)
	$xz \rightarrow yz$	-29.9

TABLE V: Nearest neighbor tight-binding hopping matrix elements (meV) for γ -Li₂IrO₃.

γ -Li ₂ IrO ₃	X_A	X_B	Y_A	Y_B	Z_A	Z_B	Z_C
$xy \rightarrow xy$	91.4	91.4	91.4	91.4	-319.7	-319.7	-17.1
$xz \rightarrow xz$	69.2	69.2	-168.3	-168.3	91.8	91.8	77.4
$yz \rightarrow yz$	-168.3	-168.3	69.2	69.2	91.8	91.8	77.4
$xy \rightarrow xz$	-262.5	262.5	4.2	-4.2	63.9	-63.9	-18.7
$xz \rightarrow xy$	-240.5	240.6	76.5	-76.5	63.9	-63.9	18.7
$xy \rightarrow yz$	4.2	-4.2	-262.5	262.5	63.9	-63.9	-18.7
$yz \rightarrow xy$	76.5	-76.5	-240.5	240.6	63.9	-63.9	18.7
$xz \rightarrow yz$	-60.2	-60.2	-10.6	-10.6	132.8	132.8	294.1
$yz \rightarrow xz$	-10.6	-10.6	-60.2	-60.2	132.8	132.8	294.1

Appendix B: Optical conductivity with spin polarized to a direction

In order to compare the dependence of the optical conductivity along various spin directions in the zigzag mag-

netic configuration, we show the results for spins along a and c direction in Fig. 11. The results show that the σ_c component doesn't depend significantly on the spin

TABLE VI: Hopping parameters for the on-site terms (meV) for α -Li₂IrO₃ for the recently available single-crystal structure from Ref. 37.

$xy \rightarrow xy$	-401.8
$xz \rightarrow xz$	-517.4
$yz \rightarrow yz$	-517.4
$xy \rightarrow xz$	-39.0
$xz \rightarrow yz$	-39.0
$xz \rightarrow yz$	-33.5

TABLE VII: Nearest neighbor tight-binding hopping matrix elements (meV) for α -Li₂IrO₃ for the recently available single-crystal structure from Ref. 37.

α -Li ₂ IrO ₃	X	Y	Z
$xy \rightarrow xy$	70.2	70.2	-139.3
$xz \rightarrow xz$	83.6	-124.0	77.7
$yz \rightarrow yz$	-124.0	83.6	77.7
$xy \rightarrow xz$	239.0	-34.9	-30.7
$xz \rightarrow xy$	239.0	-34.9	-30.7
$xy \rightarrow yz$	-34.9	239.0	-30.7
$yz \rightarrow xy$	-34.9	239.0	-30.7
$xz \rightarrow yz$	-38.6	-38.6	285.5
$yz \rightarrow xz$	-38.6	-38.6	285.5

polarized direction, while σ_a and σ_b are more sensitive to it.

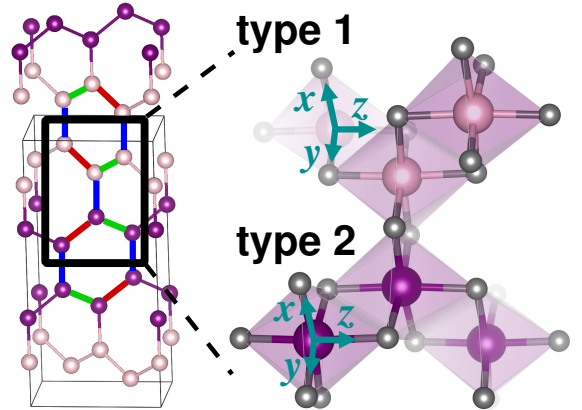


FIG. 10: (Color online) Local octahedral environment of (a) type 1 and (b) type 2 in γ -Li₂IrO₃. (n_1 , n_2 , n_3) correspond to (y, z, x) and (z, x, y) for X and Y bonds, respectively.

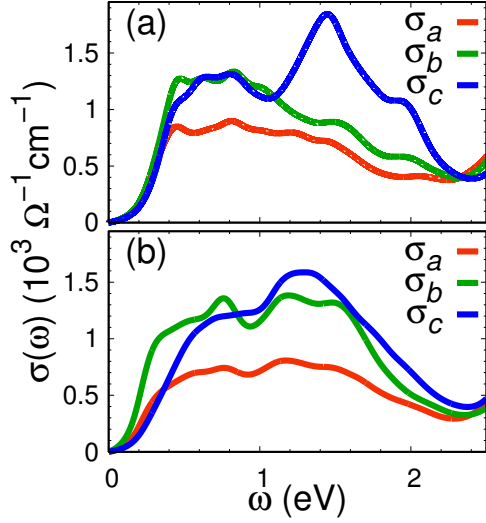


FIG. 11: (Color online) Optical conductivity tensor components with spin polarization (a) along c and (b) along a in the zigzag configuration.

- ¹ A. Kitaev, Anyons in an exactly solved model and beyond, *Ann. Phys.* **321**, 2 (2006).
- ² G. Jackeli and G. Khaliullin, Mott Insulators in the Strong Spin-Orbit Coupling Limit: From Heisenberg to a Quantum Compass and Kitaev Models, *Phys. Rev. Lett.* **102**, 017205 (2009).
- ³ J. Chaloupka, G. Jackeli, and G. Khaliullin, Kitaev-Heisenberg Model on a Honeycomb Lattice: Possible Exotic Phases in Iridium Oxides $A_2\text{IrO}_3$, *Phys. Rev. Lett.* **105**, 027204 (2010).
- ⁴ Y. Yamaji, Y. Nomura, M. Kurita, R. Arita, and M. Imada, First-Principles Study of the Honeycomb-Lattice Iridates Na_2IrO_3 in the Presence of Strong Spin-Orbit Interaction and Electron Correlations, *Phys. Rev. Lett.* **113**, 107201 (2014).
- ⁵ V. M. Katukuri, S. Nishimoto, V. Yushankhai, A. Stoyanova, H. Kandpal, S. Choi, R. Coldea, I. Rousochatzakis, L. Hozoi, and J. van den Brink, Kitaev interactions between $j = 1/2$ moments in honeycomb Na_2IrO_3 are large and ferromagnetic: insights from *ab initio* quantum chemistry calculations, *New J. Phys.* **16**, 013056 (2014).
- ⁶ J. G. Rau, E. K.-H. Lee, and H.-Y. Kee, Generic Spin Model for the Honeycomb Iridates beyond the Kitaev Limit, *Phys. Rev. Lett.* **112**, 077204 (2014).
- ⁷ J. Reuther, R. Thomale, and S. Rachel, Spiral order in the honeycomb iridate Li_2IrO_3 , *Phys. Rev. B* **90**, 100405 (2014).
- ⁸ I. I. Mazin, H. O. Jeschke, K. Foyevtsova, R. Valentí, and D. I. Khomskii, Na_2IrO_3 as a Molecular Orbital Crystal, *Phys. Rev. Lett.* **109**, 197201 (2012).
- ⁹ K. Foyevtsova, H. O. Jeschke, I. I. Mazin, D. I. Khomskii, and R. Valentí, *Ab initio* analysis of the tight-binding parameters and magnetic interactions in Na_2IrO_3 , *Phys. Rev. B* **88**, 035107 (2013).
- ¹⁰ Y. Li, K. Foyevtsova, H. O. Jeschke, and R. Valentí, Analysis of the optical conductivity for $A_2\text{IrO}_3$ ($A=\text{Na}, \text{Li}$) from first principles, *Phys. Rev. B* **91**, 161101 (2015).
- ¹¹ T. Takayama, A. Kato, R. Dinnebier, J. Nuss, H. Kono, L. S. I. Veiga, G. Fabbri, D. Haskel, and H. Takagi, Hyperhoneycomb Iridate $\beta\text{-Li}_2\text{IrO}_3$ as a Platform for Kitaev Magnetism, *Phys. Rev. Lett.* **114**, 077202 (2015).
- ¹² A. Biffin, R. D. Johnson, S. Choi, F. Freund, S. Manni, A. Bombardi, P. Manuel, P. Gegenwart, and R. Coldea, Unconventional magnetic order on the hyperhoneycomb Kitaev lattice in $\beta\text{-Li}_2\text{IrO}_3$: Full solution via magnetic resonant x-ray diffraction, *Phys. Rev. B* **90**, 205116 (2014).
- ¹³ K. A. Modic, T. E. Smidt, I. Kimchi, N. P. Breznay, A. Biffin, S. Choi, R. D. Johnson, R. Coldea, P. Watkins-Curry, G. T. McCandless, J. Y. Chan, F. Gandara, Z. Islam, A. Vishwanath, A. Shekhter, R. D. McDonald, and J. G. Analytis, Realization of a three-dimensional spin-anisotropic harmonic honeycomb iridate, *Nat. Commun.* **5**, 4203 (2014).
- ¹⁴ A. Biffin, R. D. Johnson, I. Kimchi, R. Morris, A. Bombardi, J. G. Analytis, A. Vishwanath, and R. Coldea, Noncoplanar and Counterrotating Incommensurate Magnetic Order Stabilized by Kitaev Interactions in $\gamma\text{-Li}_2\text{IrO}_3$, *Phys. Rev. Lett.* **113**, 197201 (2014).
- ¹⁵ S. Mandal and N. Surendran, Exactly solvable Kitaev model in three dimensions, *Phys. Rev. B* **79**, 024426 (2009).
- ¹⁶ I. Kimchi, J. G. Analytis, and A. Vishwanath, Three-dimensional quantum spin liquids in models of harmonic-honeycomb iridates and phase diagram in an infinite- D approximation, *Phys. Rev. B* **90**, 205126 (2014).
- ¹⁷ E. K.-H. Lee, R. Schaffer, S. Bhattacharjee, and Y. B. Kim, Heisenberg-Kitaev model on the hyperhoneycomb lattice, *Phys. Rev. B* **89**, 045117 (2014).
- ¹⁸ I. Kimchi, R. Coldea, and A. Vishwanath, Unified theory of spiral magnetism in the harmonic-honeycomb iridates

- α , β , and γ - Li_2IrO_3 , Phys. Rev. B **91**, 245134 (2015).
- ¹⁹ E. K.-H. Lee, J. G. Rau, and Y. B. Kim, Two iridates, two models, and two approaches: A comparative study on magnetism in three-dimensional honeycomb materials, Phys. Rev. B **93**, 184420 (2016).
 - ²⁰ S. M. Winter, Y. Li, H. O. Jeschke, and R. Valentí, Challenges in design of Kitaev materials: Magnetic interactions from competing energy scales, Phys. Rev. B **93**, 214431 (2016).
 - ²¹ J. P. Hinton, S. Patankar, E. Thewalt, A. Ruiz, G. Lopez, N. Breznay, A. Vishwanath, J. Analytis, J. Orenstein, J. D. Koralek, and I. Kimchi, Photoexcited states of the harmonic honeycomb iridate γ - Li_2IrO_3 , Phys. Rev. B **92**, 115154 (2015).
 - ²² N. Nembrini, S. Peli, F. Banfi, G. Ferrini, Y. Singh, P. Gegenwart, R. Comin, A. Foyevtsova, K. and DamDamasceli, A. Avella, and C. C. Giannetti, Tracking local spin-dynamics via high-energy quasi-molecular excitations in a spin-orbit Mott insulator, arXiv:1606.01667.
 - ²³ Z. V. Pchelkina, S. V. Streltsov, and I. I. Mazin, Spectroscopic signatures of molecular orbitals on a honeycomb lattice, arXiv:1607.08847.
 - ²⁴ P. Blaha, K. Schwarz, G. K. H. Madsen, D. Kvasnicka, and J. Luitz, WIEN2k, An Augmented Plane Wave Plus Local Orbitals Program for Calculating Crystal Properties (Karlheinz Schwarz, Techn. Universität Wien, Austria) (2001).
 - ²⁵ J. P. Perdew, K. Burke, and M. Ernzerhof, Generalized Gradient Approximation Made Simple, Phys. Rev. Lett. **77**, 3865 (1996).
 - ²⁶ V. I. Anisimov, I. V. Solovyev, M. A. Korotin, M. T. Czyżyk, and G. A. Sawatzky, Density-functional theory and NiO photoemission spectra, Phys. Rev. B **48**, 16929 (1993).
 - ²⁷ M. Aichhorn, L. Pourovskii, V. Vildosola, M. Ferrero, O. Parcollet, T. Miyake, A. Georges, and S. Biermann, Dynamical mean-field theory within an augmented plane-wave framework: Assessing electronic correlations in the iron pnictide LaFeAsO , Phys. Rev. B **80**, 085101 (2009).
 - ²⁸ J. Ferber, K. Foyevtsova, H. O. Jeschke, and R. Valentí, Unveiling the microscopic nature of correlated organic conductors: The case of κ -(ET)₂ $\text{Cu}[\text{N}(\text{CN})_2]\text{Br}_x\text{Cl}_{1-x}$, Phys. Rev. B **89**, 205106 (2014).
 - ²⁹ C. Ambrosch-Draxl and J. O. Sofo, Linear optical properties of solids within the full-potential linearized augmented planewave method, Comput. Phys. Commun. **175**, 1 (2006).
 - ³⁰ J. Ferber, Y.-Z. Zhang, H. O. Jeschke, and R. Valentí, Analysis of spin-density wave conductivity spectra of iron pnictides in the framework of density functional theory, Phys. Rev. B **82**, 165102 (2010).
 - ³¹ R. D. Johnson, S. C. Williams, A. A. Haghighirad, J. Singleton, V. Zapf, P. Manuel, I. I. Mazin, Y. Li, H. O. Jeschke, R. Valentí, and R. Coldea, Monoclinic crystal structure of α - RuCl_3 and the zigzag antiferromagnetic ground state, Phys. Rev. B **92**, 235119 (2015).
 - ³² B. H. Kim, G. Khaliullin, and B. I. Min, Electronic excitations in the edge-shared relativistic Mott insulator: Na_2IrO_3 , Phys. Rev. B **89**, 081109 (2014).
 - ³³ B. H. Kim, G. Khaliullin, and B. I. Min, Magnetic Couplings, Optical Spectra, and Spin-Orbit Exciton in $5d$ Electron Mott Insulator Sr_2IrO_4 , Phys. Rev. Lett. **109**, 167205 (2012).
 - ³⁴ D. Baeriswyl, C. Gros, and T. M. Rice, Landau parameters of almost-localized Fermi liquids, Phys. Rev. B **35**, 8391 (1987).
 - ³⁵ C. H. Sohn, H.-S. Kim, T. F. Qi, D. W. Jeong, H. J. Park, H. K. Yoo, H. H. Kim, J.-Y. Kim, T. D. Kang, D.-Y. Cho, G. Cao, J. Yu, S. J. Moon, and T. W. Noh, Mixing between $J_{\text{eff}} = \frac{1}{2}$ and $\frac{3}{2}$ orbitals in Na_2IrO_3 : A spectroscopic and density functional calculation study, Phys. Rev. B **88**, 085125 (2013).
 - ³⁶ R. Comin, G. Levy, B. Ludbrook, Z.-H. Zhu, C. N. Veenstra, J. A. Rosen, Y. Singh, P. Gegenwart, D. Stricker, J. N. Hancock, D. van der Marel, I. S. Elfimov, and A. Damascelli, Na_2IrO_3 as a Novel Relativistic Mott Insulator with a 340-meV Gap, Phys. Rev. Lett. **109**, 266406 (2012).
 - ³⁷ F. Freund, S. C. Williams, R. D. Johnson, R. Coldea, P. Gegenwart, and A. Jesche, Single crystal growth from separated educts and its application to lithium transition-metal oxides, arXiv:1604.04551 (2016).